Mineralogical Magazine, April 2018, Vol. 82(2), pp. 313–327

Rare-earth crystal chemistry of thalénite-(Y) from different environments

Markus B. Raschke[1,*], Evan J. D. Anderson[1], Jason Van Fosson[2], Julien M. Allaz[3], Joseph R. Smyth[2], Radek Škoda[4], Philip M. Persson[5] and Randy Becker[6]

[1] Department of Physics, Department of Chemistry, and JILA, University of Colorado, Boulder, Colorado 80309, USA
[2] Department of Geological Sciences, University of Colorado, Boulder, Colorado 80309, USA
[3] Inst. für Geochemie und Petrologie, ETH Zürich, Clausiusstrasse 25, 8092 Zürich, Switzerland
[4] Department of Geological Sciences, Masaryk University, Kotlářská 2, CZ-61137 Brno, Czech Republic
[5] Department of Geology and Geological Engineering, Colorado School of Mines, Golden, Colorado 80401, USA
[6] Yakima, Washington 98908, USA

[*Received 23 February 2017; Accepted 1 June 2017; Associate Editor: Stuart Mills*]

ABSTRACT

Thalénite-(Y), ideally $Y_3Si_3O_{10}F$, is a heavy-rare-earth-rich silicate phase occurring in granite pegmatites that may help to illustrate rare-earth element (*REE*) chemistry and behaviour in natural systems. The crystal structure and mineral chemistry of thalénite-(Y) were analysed by electron microprobe analysis, X-ray diffraction and micro-Raman spectroscopy from a new locality in the peralkaline granite of the Golden Horn batholith, Okanogan County, Washington State, USA, in comparison with new analyses from the White Cloud pegmatite in the Pikes Peak batholith, Colorado, USA. The Golden Horn thalénite-(Y) occurs as late-stage sub-millimetre euhedral bladed transparent crystals in small miarolitic cavities in an arfvedsonite-bearing biotite granite. It exhibits growth zoning with distinct heavy-rare-earth element (*HREE*) *vs*. light-rare-earth element (*LREE*) enriched zones. The White Cloud thalénite-(Y) occurs in two distinct anhedral and botryoidal crystal habits of mostly homogenous composition. In addition, minor secondary thalénite-(Y) is recognized by its distinct Yb-rich composition (up to 0.8 atoms per formula unit (apfu) Yb). Single-crystal X-ray diffraction analysis and structure refinement reveals Y-site ordering with preferential *HREE* occupation of Y2 *vs*. Y1 and Y3 *REE* sites. Chondrite normalization shows continuous enrichment of *HREE* in White Cloud thalénite-(Y), in contrast to Golden Horn thalénite-(Y) with a slight depletion of the heaviest *REE* (Tm, Yb and Lu). The results suggest a hydrothermal origin of the Golden Horn miarolitic thalénite-(Y), compared to a combination of both primary magmatic followed by hydrothermal processes responsible for the multiple generations over a range of spatial scales in White Cloud thalénite-(Y).

Keywords: thalénite-(Y), Golden Horn batholith, North Cascades, White Cloud pegmatite, South Platte pegmatite district, Pikes Peak batholith, X-ray structure refinement, electron microprobe analysis, Raman spectroscopy.

Introduction

Thalénite-(Y), ideally $Y_3Si_3O_{10}F$, is a monoclinic *REE* silicate that was first described by Benedicks (1898, 1900), from the Österby granite pegmatite, Dalarna, Sweden, and named in honour of the Swedish physicist Tobias R. Thalén (1827–1905). It has been identified subsequently in only ca. 10 other localities worldwide, primarily in niobium-yttrium-fluorine (NYF) granitic pegmatites, and some other igneous suites (Adams *et al.*, 1962; Vorma *et al.*, 1966; Nagashima and Kato, 1966; Adams and Sharp, 1972; Kornev *et al.*, 1972;

*E-mail: markus.raschke@colorado.edu
https://doi.org/10.1180/minmag.2017.081.044

Fitzpatrick and Pabst, 1986; Griffin *et al.*, 1979; Kristiansen, 1993; Voloshin and Pakhomovskii, 1997; Minakawa *et al*., 1999; Kozireva *et al.*, 2004; Gonzáles del Tánago *et al.*, 2006; Raade and Kristiansen, 2009; Stepanov *et al*., 2012). Thalénite-(Y) was recently re-examined from different localities (Škoda *et al.*, 2015), including the type material, demonstrating that F dominates over OH. 'Fluorthalénite-(Y)' was thus redefined as thalénite-(Y) by the Commission on New Minerals, Nomenclature and Classification of the International Mineralogical Association (IMA 14-D, Williams, 2014) as the F-dominant parent compound.

Thalénite-(Y) is part of the thortveitite group (thortveitite $(Sc,Y)_2Si_2O_7$, rowlandite-(Y) $Y_4Fe(Si_2O_7)_2F_2$ and yttrialite $(Y,Th)_2Si_2O_7$)). It occurs as tabular to prismatic crystals of greasy lustre and biaxial (–) birefringence, with conchoidal fracture, hardness between 6 and 6.5 and specific gravity of ~4.2. It is monoclinic with space group $P2_1/n$ with $a \approx 7.30$, $b \approx 11.12$, $c \approx 10.37$ Å, $\beta \approx 97°$ and $Z = 4$. It is commonly metamict when enriched in actinides (Fitzpatrick and Pabst, 1986).

Despite the range of studies from several localities (see Škoda *et al.*, 2015 and references therein), the question of the necessary geochemical environment for its formation is still poorly constrained for both primary magmatic thalénite-(Y), as well as its formation by replacement and alteration, possibly from britholite-(Y) (Minakawa *et al.*, 1999). Thalénite-(Y) is generally rare, but where it occurs it is often abundant, and often associated with other *REE* minerals such as fergusonite $(REE)NbO_4$, gadolinite $(REE)_2FeBe_2Si_2O_{10}$ and allanite-group minerals (Armbruster *et al*., 2006; Mills *et al*., 2009; Bačík *et al*., 2017), as well as with zircon and magnetite. However, it remains an uncommon mineral, even in pegmatites of NYF affinity and high abundance of *HREE* and F, which suggests that other environmental factors besides *P-T* conditions and elevated *REE* and F control thalénite-(Y) crystallization.

The present study investigates the crystal chemistry of thalénite-(Y) from a new occurrence in the peralkaline granite of the Golden Horn batholith, North Cascade Mountains, Washington State, USA, with a focus on chemical composition and crystal structure. Results are compared with detailed analyses of thalénite-(Y) from the White Cloud pegmatite, South Platte District, Colorado, USA. To address the F and OH substitution we performed Raman spectroscopy for the identification of the crystal OH groups.

Occurrence and geological setting

Golden Horn thalénite-(Y)

The Golden Horn batholith is a shallow peralkaline granitic intrusion of Eocene age (47–50 Ma) (Misch, 1966; Stull, 1969; Boggs, 1984; Eddy *et al.*, 2016). There are four phases of granite intrusions in the batholith: a peralkaline arfvedsonite granite, a less alkaline transitional 'border granite', and two different types of biotite granites (Boggs, 1984). The granites are unusually rich in *REE* minerals and rare Zr-bearing silicate minerals.

A wide range of rare *REE* minerals have been noted in small miarolitic cavities in the Golden Horn batholith, primarily *REE*-carbonates 'bastnäsite' and 'synchysite', allanite-(Ce), betafergusonite, calciohilairite, chevkinite, euxenite, gadolinite, gagarinite, kainosite, okanoganite and pyrochlore-group minerals (Becker, 1991; Boggs, 1980, 1984, 1988). The thalénite-(Y) studied was found in a single small talus boulder in the centre west face of Kangaroo Ridge, south east of Washington Pass. Kangaroo Ridge, the likely source for this talus boulder, is composed predominantly of arfvedsonite granite with minor biotite granite.

The thalénite-(Y)-bearing talus boulder is mostly medium-grained peralkaline arfvedsonite granite composed of white microcline, arfvedsonite, and minor annite and colourless quartz, with annite-bearing miarolitic cavities. When intersecting a cavity, arfvedsonite forms euhedral crystals. The miarolitic cavities are up to 2 cm in diameter, and contain uncommon thalénite-(Y) crystals up to ~2 mm in size which occur as clusters, or sometimes as smaller single crystals (Fig. 1*a*,*c*). Crystals are colourless to light pink, transparent to translucent, and have a bright lustre. They are associated with well-formed crystals of microcline, arfvedsonite, quartz, annite and rarely wulfenite, zircon, a pyrochlore-group mineral and *REE* carbonates. Late-stage annite is abundant in some of the cavities as colour zoned crystals ranging from colourless to brown and black.

White Cloud thalénite-(Y)

Following the first description of thalénite-(Y) in Colorado at the Snowflake pegmatite in the South Platte NYF pegmatite district (Adams *et al.*, 1962), thalénite-(Y) was described from the White Cloud pegmatite, situated ~10 km east of the village of Buffalo Creek (Adams and Sharp, 1972). The White Cloud pegmatite is an asymmetric elliptical

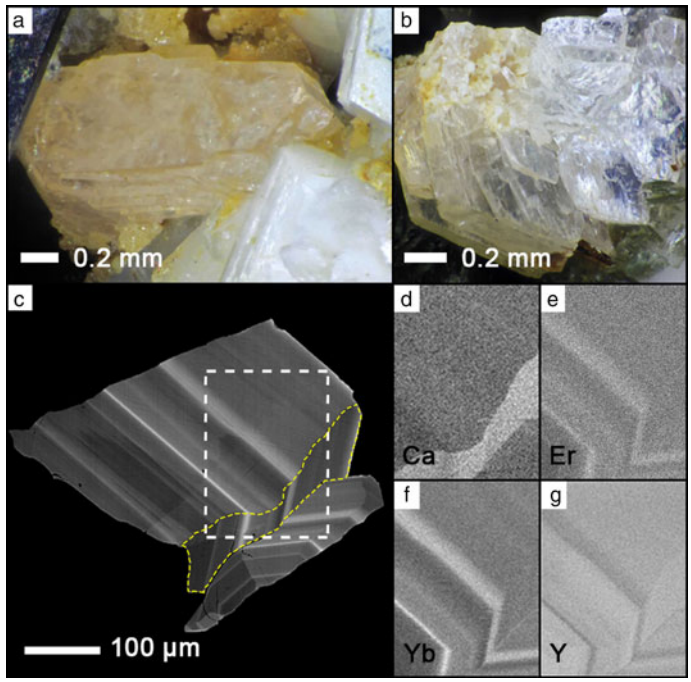

FIG. 1. (*a*,*b*) Thalénite-(Y) from miaorolitic cavities from the Golden Horn batholith, Washington, USA (photos courtesy of Rudy Tschernich). (*c*) Back-scatter electron (BSE) image of thalénite-(Y) with distinct oscillatory zoning. White dashed box corresponds to the element distribution maps of (*d*) Ca*K*α, (*e*) Er*L*α, (*f*) Yb*L*α and (*g*) Y*L*α. The yellow dashed region in (*c*) highlights a region of unusually high Ca content visible in (*d*).

body ~100 m × 40 m across, zoned, and geochemically complex. It is hosted in the northern part of the ~1.08 Ga A-type Pikes Peak batholith, within subsolidus two-feldspar quartz monzonite, in turn surrounded by one-feldspar hypersolvus granite (Haynes, 1965; Simmons and Heinrich, 1975; Simmons and Heinrich, 1980; Smith *et al.*, 1999; Frost and Frost, 1997; Adams and Sharp, 1972).

The White Cloud pegmatite is mineralogically distinct from most known South Platte pegmatites, with a diversity of *REE* species, including *REE* silicates. It is a well-zoned body consisting of major quartz and perthitic alkali feldspar (locally albitized), with minor biotite, and fluorite of variable Y + *REE* content (Wayne, 1986). The *REE* minerals include allanite-(Ce), gadolinite-(Y), fergusonite-(Y) and *REE*-rich zircon (var. cyrtolite), most of which occur with fluorite in discrete zones in the pegmatite (Haynes, 1965; Wayne, 1986). Haynes (1965) and Wayne (1986) suggested two hydrothermal alteration episodes in the White Cloud pegmatite. First, gadolinite is replaced by Y-rich fluorite, *REE*-carbonates and fluocerite-(Ce), and perthitic alkali feldspar is replaced by albite. Second, biotite is altered into Fe-oxide and clay minerals. Thalénite-(Y) occurs both as intergrowths with yttrofluorite, as well as associated with quartz and feldspar (Adams and Sharp, 1972). The texture varies from dense, dull-grey decimetre-sized aggregates of nodular texture associated with Y-rich fluorite, gadolinite, 'bastnäsite', 'synchysite', 'allanite', thorite and zircon, to areas in which irregular textured Y-rich fluorite is associated with the aforementioned *REE* minerals with minor blebs and veinlets of thalénite-(Y) (Adams and Sharp, 1972; Wayne, 1986). Thalénite-(Y)-bearing samples were collected from three *in situ* locations in the northwest wall of the pegmatite quarry. It occurs in pods in the quartz-perthite-fluorite zone, immediately adjacent to the quartz-microcline core zone.

Petrographic analysis revealed two types of thalénite-(Y): large anhedral grains up to a millimetre in size, or finely-distributed swarms with a grain size of tens of micrometres, intergrown with the Y-rich fluorite. Both types are pink to colourless with first-order birefringence.

Material and analytical methods

Electron microprobe (EMP) analysis and WDS X-ray element mapping of thalénite-(Y) were performed primarily on a JEOL JXA-8600 instrument of four individual grains from the Golden Horn batholith and in two thin sections WC01 and WC02 from the White Cloud pegmatite (for details of analytical conditions see Supplementary material).

Four individual grain mounts of crystal fragments from the Golden Horn thalénite-(Y) were analysed, with 36 analyses in grain 1 (Fig. 1*c*), 22 from grain 2, 12 from grain 3 and 5 from grain 4. Sixty-six analyses were performed in the two White Cloud thin sections WC01 and WC02, with representative areas and locations indicated in Figs 2 and 3.

Following the microprobe analysis five grains were extracted from selected sample areas for subsequent correlative X-ray diffraction (XRD) analysis: Golden Horn crystal fragment GH-01 from grain 1; crystallites WC-G5, WC-X5 and WC-X7 drilled from thin sections WC02 in or near regions analysed by EMP; and a sample from Hundholmen, Tysfjord, Norway (RS104), previously analysed by EMP in Škoda *et al.* (2015). Due to minor inconsistencies with high Si and low *REE* content on the JEOL JXA-8600, control analyses were performed on a new JEOL JXA-8230 instrument on selected samples that became available only after the XRD sample extraction (see Supplementary material).

Single-crystal XRD was performed on a Bruker P4 four circle diffractometer equipped with a point detector, an APEX II CCD detector, and a rotating Mo-anode generator operating at 50 kV and 250 mA with a graphite monochromator. Unit-cell parameters were refined from centring angles for 30 strong reflections with $10° < 2\theta < 30°$ each in both positive and negative 2θ regions using the point-detector. For intensity data, the maximum 2θ angle was 70°. Single-crystal XRD data were measured using the CCD detector, and data collection parameters are listed in Table 1.

Micro-Raman spectroscopy on polished sections was performed on an upright microscope (Olympus BH51), with 632 nm HeNe laser excitation at 1 mW, 50x objective of NA = 0.8, imaging spectrograph (Princeton Instruments spectrometer Acton SP500, with PIXIS 100 liquid nitrogen cooled CCD camera, calibrated on multiple spectral lines using an He-lamp).

Results

Chemical composition

Quantitative EMP analyses of thalénite-(Y) are summarized in Table 2, and complemented by X-ray element mapping shown in Figs 1 to 3. Backscattered electron images show pronounced oscillatory zoning for the Golden Horn thalénite-(Y) (Fig. 1*c*), which correlates with an increase in Yb and Er, and a decrease in Y (Fig. 1*d–g*; Table 2).

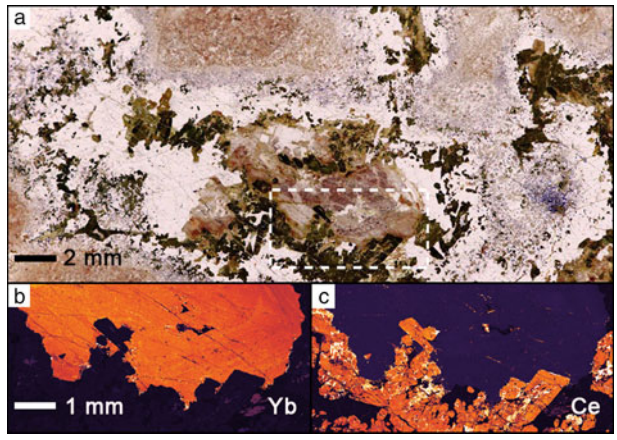

FIG. 2. (*a*) White Cloud thalénite-(Y) rock thin section (plane-polarized light), with gadolinite (green), allanite-(Ce) (black fluorite (colourless) and thalénite-(Y) (pink). The area of the dashed box is shown in the Yb$L\alpha$ distribution map (*b*) highlighting the anhedral mostly homogenous thalénite-(Y) crystal with high Yb$L\alpha$ values shown in orange. The Ce$L\alpha$ distribution map (*c*) emphasizes adjacent gadolinite in brownish-green and allanite-(Ce) in darker black in (*a*).

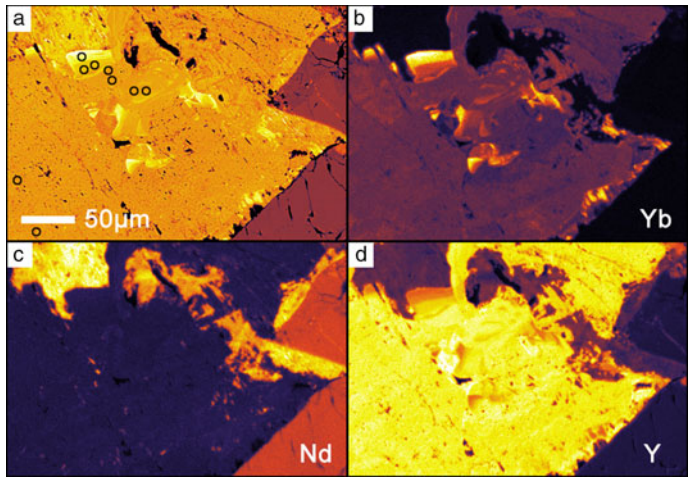

FIG. 3. BSE and false-colour elemental maps showing anhedral and heterogeneous thalénite-(Y) from White Cloud. (*a*) BSE image, (*b*) Yb*Lα*, (*c*) Nd*Lα* and (*d*) Y*Lα*. Allanite is seen in the bottom right with gadolinite in the top left. Dark open circles in (*a*) are selected points for analysis as shown in Table 2. Notice the Yb-enrichment in (*b*).

In addition, a distinct Ca-rich domain is observed (Fig. 1*d*). In contrast, element mapping in thalénite-(Y) from the White Cloud shows large areas of relatively homogeneous euhedral thalénite-(Y) crystals with minor variation in content of Y and heavy *REE* (*HREE*: Tb to Lu) (Fig. 2*b*, Table 2), alternate with regions of a botryoidal phase. Locally, along the rim of some large grains, a distinct enrichment in the heaviest *REE* is observed (Er to Lu; Fig 3*a*,*b*).

The columns in Table 2, 'High Ti', 'High Yb', 'Low Yb' and 'High Y' correspond to different zones highlighting distinct zonal composition in the Golden Horn thalénites as observed in the different crystal grains 1 to 4. For example: 'High Yb' corresponds to similar regions observed in grains 1, 2 and 4; 'High Ti' was a region observed in grain 3; 'Low Yb' was found in grains 3 and 4; and 'High Y' in grains 1 and 4. The columns for the White Cloud thalénites highlight zonal

TABLE 1. Crystal structure refinement data for thalénite-(Y).

Samples	$Y_3Si_3O_{10}F$*	GH-01	WC-G5	WC-X5	WC-X7	RS104
Unit-cell parameters:						
a (Å)	7.3038	7.3249(11)	7.346(4)	7.3226(9)	7.3251(7)	7.330(4)
b (Å)	11.1247	11.1330(14)	11.194(7)	11.1808(13)	11.1725(10)	11.266(8)
c (Å)	10.3714	10.3792(19)	10.412(6)	10.3763(13)	10.4192(10)	10.477(7)
β (°)	97.235	97.292(15)	97.338(3)	97.417(9)	97.504(7)	97.12(4)
V (Å^3)	835.99	839.6(2)	849.2(10)	842.43(18)	845.40(14)	858.5(10)
No. reflections		9021	6202	10,904	10,205	3984
No. unique refl.		2415	1466	2360	2743	1711
No. refl. $I > 2\sigma(I)$		1758	1012	1310	1261	812
R_{int}		0.0673	0.089	0.1816	0.1272	0.1105
R_1		0.0499	0.0492	0.0773	0.0984	0.0766
w*R*		0.1373	0.1402	0.2089	0.2206	0.2016
Parameters refined		162	162	162	162	162

*Schleid and Müller-Bunz (1998)

TABLE 2. Representative averages of EMP analyses for Golden Horn and White Cloud as well as data from White Cloud (WC) by Škoda *et al.* (2015). Atomic proportions are calculated assuming a total of 10 oxygens, a fixed Si content of 3 and a fixed F of 1 (apfu).

	Golden Horn thalénite-(Y)						White Cloud thalénite-(Y)						WC Škoda[a]
	High Ti	High Yb	Low Yb	High Y	Range	Bulk Avg.	High Ca	Low Ca	Highest Yb	High Yb	Range	Bulk Avg.	
Wt.% oxide													
SO_3	<0.02	0.01	<0.02	0.02	<0.01–0.05	0.03	0.06	0.05	0.03	0.04	<0.01–0.29	0.08	n/a
P_2O_5	0.22	0.26	0.23	0.32	0.16–0.54	0.29	<0.04	0.02	<0.05	<0.05	<0.04–0.08	0.06	n/a
SiO_2	31.36	30.64	31.32	32.21	29.61–32.45	31.55	30.05	30.37	28.36	29.56	28.10–31.85	30.13	31.11
TiO_2	0.21	0.05	0.19	0.19	<0.01–0.25	0.07	0.01	<0.04	<0.05	<0.04	<0.04–0.07	0.06	n/a
ThO_2	0.02	0.01	0.01	<0.03	<0.03–0.12	0.06	<0.04	<0.05	0.03	<0.09	<0.04–0.12	0.09	bdl
UO_2	<0.02	<0.04	<0.02	<0.02	<0.02	<0.03	0.04	<0.07	<0.06	<0.06	<0.03–0.12	0.10	bdl
Al_2O_3	<0.01	<0.02	<0.02	<0.01	<0.01	<0.02	0.21	<0.01	0.10	<0.05	<0.01–0.50	0.21	n/a
Fe_2O_3	0.01	0.09	0.01	0.07	<0.01–0.22	0.07	0.37	<0.02	0.01	<0.02	<0.01–0.70	0.20	n/a
Y_2O_3	46.07	42.94	46.24	50.08	39.62–50.98	46.95	40.98	43.82	30.37	39.11	29.73–46.067	42.28	45.43
La_2O_3	0.07	0.07	0.07	0.03	<0.02–0.24	0.13	0.01	<0.08	0.08	<0.09	<0.05–0.14	0.10	bdl
Ce_2O_3	0.36	0.20	0.35	0.14	<0.02–0.89	0.31	0.26	<0.05	0.02	<0.07	<0.04–0.80	0.30	0.59
Pr_2O_3	0.11	0.03	0.10	0.03	<0.03–0.19	0.10	0.08	<0.04	<0.08	<0.10	<0.06–0.28	0.15	0.14
Nd_2O_3	0.84	0.16	0.79	0.22	<0.02–0.98	0.30	0.75	0.16	0.16	0.15	0.07–2.30	0.66	1.42
Sm_2O_3	1.11	0.15	1.05	0.23	<0.02–1.15	0.27	0.85	0.48	0.07	0.28	0.00–2.28	0.81	1.18
Eu_2O_3	0.08	0.07	0.09	0.04	<0.03–0.16	0.07	0.26	0.32	0.11	0.30	0.00–0.47	0.27	n/a
Gd_2O_3	3.18	0.67	3.05	0.89	0.24–3.28	0.96	1.89	1.82	0.49	0.84	0.41–3.67	1.88	2.28
Tb_2O_3	0.75	0.25	0.73	0.36	0.2–0.76	0.33	0.51	0.57	0.14	0.35	0.12–0.87	0.53	0.50
Dy_2O_3	5.57	3.62	5.50	4.09	3.24–5.62	4.03	4.15	4.79	2.24	3.91	2.01–5.75	4.36	4.04
Ho_2O_3	1.15	1.25	1.14	1.17	1.09–1.44	1.23	0.95	1.16	0.80	1.13	0.76–1.25	1.01	0.96
Er_2O_3	3.18	6.41	3.16	4.37	3.12–6.72	5.23	3.83	4.45	6.27	5.75	3.25–6.35	4.17	3.47
Tm_2O_3	0.36	1.30	0.36	0.58	0.35–1.34	0.84	0.67	0.86	2.05	1.36	0.4033–2.11	0.78	0.65
Yb_2O_3	1.55	7.46	1.55	2.66	1.52–7.85	4.17	6.07	6.62	22.83	12.20	3.18–23.65	7.06	4.98
Lu_2O_3	0.05	0.56	0.07	0.15	<0.03–0.6	0.28	0.95	0.96	3.81	1.58	0.42–4.37	1.06	0.94
MgO	<0.01	<0.01	<0.02	<0.01	<0.01	<0.01	<0.04	<0.02	<0.03	<0.02	<0.01	0.06	n/a
CaO	0.48	0.39	0.48	0.31	0.14–0.66	0.38	1.11	0.03	0.06	0.03	0.020–1.29	0.31	0.09
MnO	0.00	0.02	<0.02	0.02	<0.01–0.06	0.02	0.05	<0.02	<0.03	<0.02	<0.01–0.10	0.06	bdl
BaO	<0.02	<0.02	<0.02	<0.02	<0.02–0.04	0.04	<0.02	<0.02	<0.04	<0.02	<0.02	<0.04	n/a
SrO	<0.02	<0.03	<0.02	<0.02	<0.01–0.04	0.04	<0.04	<0.05	<0.06	<0.06	<0.01–0.04	0.04	n/a
Na_2O	<0.01	0.02	<0.02	0.02	<0.01–0.06	0.03	0.02	<0.03	<0.03	<0.03	<0.01–0.13	0.05	n/a
H_2O	n/a	n/a	n/a	n/a	n/a	n/a	n/a	n/a	n/a	n/a	n/a	n/a	0.05
F*	3.31	3.23	3.30	3.40	3.12–3.42	3.33	3.17	3.20	2.99	3.12	2.96–3.36	3.18	3.14
O = F	−1.39	−1.36	−1.39	−1.43	−1.44 to −1.31	−1.40	−1.33	−1.35	−1.26	−1.31	−1.41 to −1.25	−1.34	−1.32
Total	98.65	98.50	98.41	100.00	96.54–101.18	99.31	95.99	98.27	99.64	98.38	93.99–102.12	97.57	99.65

Atoms per formula unit													
S	<0.001	<0.003	<0.001	0.001	<0.001–0.003	0.002	0.004	<0.003	<0.003	<0.002	<0.002–0.021	0.006	n/a
P	0.018	0.022	0.018	0.025	0.013–0.044	0.023	0.000	<0.002	<0.002	<0.002	<0.002–0.003	0.005	n/a
Si (Fixed)	3	3	3	3			3	3	3	3			3.001
Ti	0.015	0.004	0.014	0.003	<0.003–0.018	0.005	0.001	<0.003	<0.003	<0.003	<0.003–0.005	0.004	n/a
Th	0.000	0.000	0.000	0.000	<0.001–0.002	0.001	<0.001	0.000	0.001	<0.001	<0.001–0.003	0.002	bdl
U	<0.001	<0.001	<0.001	<0.001	<0.001	<0.001	0.001	<0.001	<0.001	<0.001	<0.001–0.003	0.002	bdl
Y	2.345	2.237	2.357	2.482	2.137–2.508	2.375	2.177	2.303	1.709	2.112	1.666–2.378	2.238	2.332
La	0.003	0.002	0.002	0.001	<0.003–0.009	0.004	0.001	<0.004	<0.003	<0.003	<0.003–0.005	0.004	0.003
Ce	0.013	0.007	0.012	0.005	<0.003–0.031	0.011	0.010	<0.002	0.001	<0.002	<0.002–0.028	0.011	0.021
Pr	0.004	0.001	0.004	0.001	<0.005–0.007	0.003	0.003	<0.001	<0.003	<0.003	<0.001–0.010	0.006	0.005
Nd	0.029	0.005	0.027	0.007	<0.003–0.033	0.010	0.027	0.006	0.006	0.006	0.002–0.082	0.023	0.049
Sm	0.037	0.005	0.035	0.007	<0.003–0.038	0.009	0.029	0.016	0.003	0.010	<0.002–0.078	0.028	0.039
Eu	0.003	0.002	0.003	0.001	<0.001–0.006	0.002	0.009	0.011	0.004	0.011	<0.001–0.016	0.009	n/a
Gd	0.101	0.022	0.097	0.027	0.008–0.104	0.030	0.062	0.059	0.017	0.028	0.014–0.122	0.062	0.073
Tb	0.023	0.008	0.023	0.011	0.006–0.024	0.010	0.017	0.018	0.005	0.012	0.004–0.029	0.017	0.016
Dy	0.172	0.114	0.170	0.123	0.098–0.168	0.123	0.134	0.152	0.076	0.128	0.068–0.185	0.140	0.126
Ho	0.035	0.039	0.035	0.035	0.032–0.043	0.037	0.030	0.036	0.027	0.036	0.026–0.039	0.032	0.029
Er	0.095	0.197	0.095	0.128	0.094–0.214	0.156	0.120	0.138	0.208	0.183	0.100–0.2131	0.131	0.105
Tm	0.011	0.040	0.011	0.017	0.01–0.042	0.025	0.021	0.026	0.067	0.043	0.012–0.069	0.024	0.02
Yb	0.045	0.223	0.045	0.076	0.044–0.239	0.122	0.185	0.200	0.736	0.378	0.095–0.759	0.217	0.147
Lu	0.001	0.006	0.001	0.005	<0.001–0.018	0.006	0.029	0.029	0.122	0.048	0.012–0.139	0.032	0.027
Al	<0.001	<0.002	<0.002	<0.002	<0.001	<0.002	0.025	<0.002	0.012	<0.005	<0.002–0.059	0.025	n/a
Fe^{3+}	0.001	0.009	0.001	0.006	<0.001–0.016	0.006	0.028	<0.002	0.001	<0.002	<0.001–0.053	0.015	n/a
Mn^{2+}	<0.001	0.002	<0.001	0.002	<0.001–0.005	0.002	0.004	<0.002	<0.002	<0.002	<0.001–0.009	0.005	bdl
Mg	<0.001	<0.001	<0.001	<0.001	<0.001	<0.001	<0.001	<0.001	<0.001	<0.001	<0.001	0.000	n/a
Ca	0.049	0.041	0.049	0.031	0.014–0.067	0.039	0.119	0.003	0.007	0.003	0.002–0.137	0.033	0.009
Sr	<0.001	<0.002	<0.001	<0.001	<0.001–0.002	0.002	<0.002	<0.003	<0.004	<0.003	<0.002–0.002	0.002	n/a
Na	<0.001	0.001	<0.001	0.000	<0.001–0.003	0.006	0.004	<0.001	<0.001	<0.001	<0.001–0.006	0.010	n/a
Ba	<0.001	<0.001	<0.001	0.000	<0.001–0.002	0.002	<0.001	<0.001	<0.001	<0.001	<0.001	<0.001	n/a
Sum 3^+ 2^+	2.965	2.970	2.967	2.963	2.936–2.985	2.965	3.029	2.999	3.001	2.998	2.980–3.049	3.006	3.001
OH	n/a	n/a	n/a	n/a	n/a	n/a	n/a	n/a	n/a	n/a	n/a	n/a	0.042
F (Fixed)*	1	1	1	1			1	1	1	1			0.958
O (Fixed)	10	10	10	10			10	10	10	10			10
TOTAL	6.999	7.001	7.000	6.994	6.978–7.013	6.999	7.038	7.000	7.002	7.000	6.992–7.052	7.011	7.002

[a] Škoda *et al.* (2015)

*Škoda data does not reflect fixed F = 1

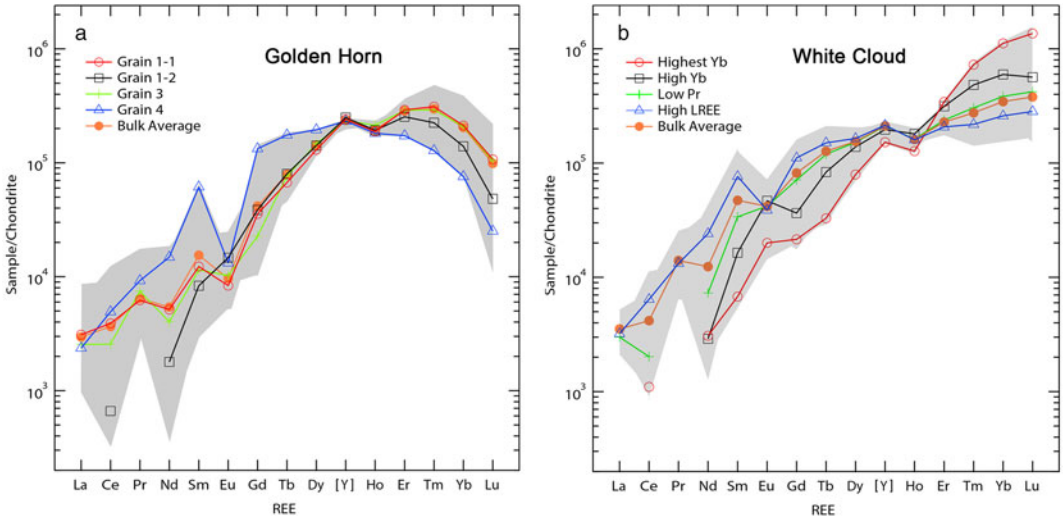

FIG. 4. (*a*) Chondrite-normalized *REE* distribution for Golden Horn thalénite-(Y) analyses with a characteristic depletion of the heaviest *HREE* (Tm to Lu). Two distinct patterns were found in grain 1, one with high levels of *HREE* (grain 1-1) and one with low *LREE* (grain 1-2). The average for grain 2 is very close to that of the bulk average and has been omitted. The bulk average values correspond to those found in Table 2. (*b*) Chondrite normalization for White Cloud thalénite-(Y), with 'Highest Yb' and 'High Yb' as shown in Table 2, and 'Low Pr' and 'High *LREE*' from selected analyses on different sample regions. The anomalously high and highest Yb content is in very localized regions of secondary thalénite-(Y) only (see Fig. 3*b*,*d*). Note the *HREE* to middle *REE* and *LREE* anti-correlation.

compositions observed in regions across the two thin sections WC01 and WC02. 'High Ca' was found in WC02 while 'Low Ca' was found in regions WC01-B2, WC01-B3M2, WC01-B3 and WC02. Both 'Highest Yb' and 'High Yb' are from region WC01-B3M2.

The mineral formulae in Table 2 are recalculated assuming a total of 10 oxygen, 3 silicon and 1 OH group, with wt.% of F reduced to full F-site occupancy (1 apfu, see Supplementary material for further details). The different columns highlight particular chemical compositions corresponding to averages of analyses of individual, or several, crystal regions of similar composition.

All thalénite-(Y) analysed are dominated by Y (1.67–2.51 apfu) and *HREE* (0.38–1.28 apfu Tb–Lu), with ~60.5–70.2 wt.% total REE_2O_3. Significant CaO is present in all samples, ranging from 0.14 to 0.66 wt.% CaO in Golden Horn and 0.02 to 1.28 wt.% CaO for White Cloud. In the Golden Horn thalénite, a local band of elevated Ca (~0.6 wt.% CaO) is identified (Fig. 1*d*). TiO_2 (<0.01 to 0.25 wt.%) and P_2O_5 (0.16 to 0.54 wt.%) in Golden Horn are inhomogeneously present. Aluminium is below the detection limit (<0.02 wt.% Al_2O_3) for Golden Horn thalénite, and present in a small amount, up to 0.50 wt.% in few analyses from White Cloud thalénite-(Y). Only traces of Mn (up to ~0.10 wt.%), Na (up to ~0.13 wt.%) and S (up to ~0.29 wt.%) are identified in both localities, and no significant U, Th, or Mg are detected.

The chemical zonation of Golden Horn thalénite-(Y) reflect the changes in *REE* distribution following the substitution vector $HREE_1Y_{-1}$ (Fig. 1*c*, *e*–*g*). *HREE*-rich and Y-poor domains in the White Cloud thalénite-(Y) are also depleted in light-*REE* (*LREE*; La to Gd) and follows a similar substitution vector $HREE_1LREE_{-1}$. The chondrite-normalized *REE* pattern as shown in Fig. 4 exhibits similar trends in comparison to previous observations (Škoda *et al.*, 2015; Voloshin and Pakkomovskii, 1997). The preference of the thalénite-(Y) structure for the smaller *HREE* cations gives rise to the continuous enrichment of the *HREE* as seen in the White Cloud thalénite-(Y). In contrast, a depletion for the heaviest *REE* is found for the Golden Horn thalénite-(Y). The near absence of an Eu-anomaly in the White Cloud thalénite-(Y) is notable, an observation which differs from the pronounced negative Eu-anomaly in the analyses by Wayne (1986).

Associated with this trend is a well-developed M-type tetrad effect as can be seen for both localities, specifically the first tetrad for grain 4,

and the third tetrad consistently for all analyses. A well-developed fourth tetrad is seen only for the Yb-rich regions in the White Cloud thalénite, yet throughout for the Golden Horn thalénite-(Y).

To highlight the substitution of lanthanides (Ln: La to Lu) for Y, Fig. 5 shows the sum of Ln plotted *vs.* Y for all analyses for Golden Horn and White Cloud thalénite-(Y). The slight deviation from the ideal slope of 1 could be due to a combination of EMP analytical uncertainties, vacancies, missing elements, and other possibly coupled substitutions, yet no such obvious cause could be identified.

Similarly to other *REE*-silicates and phosphates, a substitution of Si with P is possible and would explain the entry of Ca in the thalénite-(Y) structure through the exchange vector $REE_{-1}Si_{-1}P_1Ca_1$. While no clear correlation between Ca and P has been found, a slight anti-correlation in Fig. 6 between the sum of 3+ and 4+ cations (Si, Ti, *REE*, Al and Fe) *vs*. sum of 2+ and 5+ cations (P, Ca and Mn), suggests an $M^{2+}_{-1}T^{5+}_{-1}M^{3+}_{1}T^{4+}_{1}$ exchange vector. Additional analyses in thalénite-(Y) of higher P-content would be required to confirm this trend.

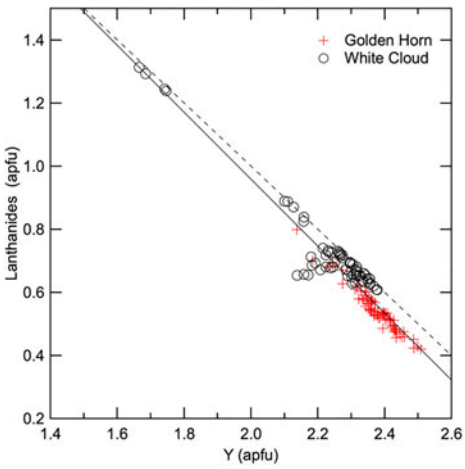

FIG. 5. Sum of Ln *vs*. Y (both apfu) for all Golden Horn and White Cloud thalénite-(Y) analyses. The dashed line marks the expected slope of –1 representing a 1:1 ideal substitution, in comparison to the solid fit line with slope $m = -1.1$ and $R^2 = 0.93$.

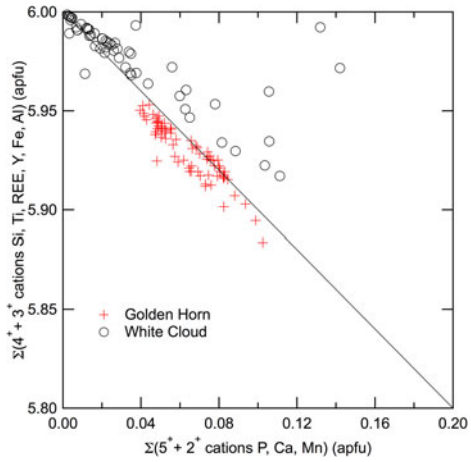

FIG. 6. Sum of 3+ and 4+ cations (Si, Ti, *REE*, Al and Fe) versus 2+ and 5+ cations (P, Ca and Mn) for all Golden Horn and White Cloud thalénite-(Y) analyses. The solid line of slope –1 shows the theoretical anti-correlation for coupled substitution exchange vector as discussed in text.

Crystallography and structure refinement

Thalénite-(Y) is a sorosilicate composed of Si_3O_{10} groups, with cations in [7] coordination, or with Y1 in [7 + 1] coordination if the longer Y1–O4 is considered. The structure is monoclinic, $P2_1/n$, with all atoms in general positions and four of each per unit cell. The crystal structure (Fig. 7) has three trivalent REE^{3+} cation sites Y1, Y2 and Y3, which are each coordinated to six oxygen and one F^- ion. The resulting $[FY_3]^{8+}$ structural element is nearly trigonal-planar. Three SiO_4 groups are connected on edge to form a trisilicate anion $[Si_3O_{10}]^{8-}$ (Kornev *et al.*, 1972; Yakubovich *et al.*, 1988; Schleid and Müller-Bunz, 1998). The REE^{3+} are then coordinated in a chelate-like fashion by the trisilicate arch via 6 + 1 (Y1) and 6 (Y2 and Y3) oxygen. Of the ten oxygen atom positions, eight are bonded to one Si, and two, O4 and O7, are bridging oxygen atoms. The other oxygen atoms each bond to two Y sites and one Si. There are no Si–F bonds, consistent with ionic bonding. Fluorine is bonded only to the *REE* atoms with one bond to each of the three Y positions. Schleid and Müller-Bunz (1998) refined the crystal structure of a pure $Y_3Si_3O_{10}F$, the synthetic equivalent to thalénite-(Y), which provides the site geometries of a pure synthetic end-member with which to compare the site geometries of our natural samples. In addition, Müller-Bunz and Schleid (2000) also report the structure refinements for synthetic $Dy_3Si_3O_{10}F$, $Ho_3Si_3O_{10}F$ and $Er_3Si_3O_{10}F$.

Unit-cell parameters were refined from the full intensity data set and corrected to a standard anhydrous quartz crystal (Angel *et al.*, 1992). Unit-cell parameters and XRD data set parameters

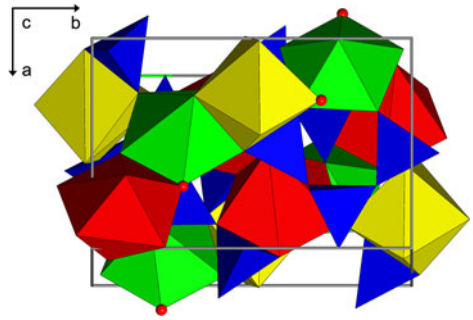

FIG. 7. The crystal structure of thalénite-(Y) (*a* vertical; *b* horizontal) showing the Si_3O_{10} trimers (blue) and the seven-coordinated Y sites, Y1 (green), Y2 (yellow) and Y3 (red). Each of the Y sites are similar in coordination and polyhedral volume and is bonded to six oxygen atoms and one fluorine (red sphere). The Y2 site appears to incorporate significantly more lanthanoid (La–Lu) cations than the other two, consistent with its deeper electrostatic potential calculated for pure $Y_3Si_3O_{10}F$.

are given in Table 1. The Golden Horn sample had a noticeably smaller unit-cell volume than that of the White Cloud samples, closer to the ideal value of 836 Å^3 (Schleid and Müller-Bunz, 1998).

The crystal structures of the five crystals were refined from single-crystal XRD data sets. For the refinements of atom positions, anisotropic displacement parameters and site occupancies the program *SHELXL-2016* (Sheldrick, 2008) was used, with ionic scattering factors for Si^{4+} and F^- (Cromer and Mann, 1968). The ionic scattering factor for O^{2-} was that of Azavant and Lichanot (1993). The Y-site occupancies were refined using an ionic Yb^{3+} scattering factor (Cromer and Mann, 1968) and the number of electrons determined by multiplying the refined occupancy by 67. For comparison we have a fixed 66.67% Y-site occupancy in the three Y-sites and let the remainder of the Y-site occupancy refine using Yb^{3+}. We obtain slightly improved *R*-factors in each case, but the differences are only marginally significant to insignificant. We refined for Si^{4+} because of the possibility of Be substitution, considering the significant presence of gadolinite in the White Cloud pegmatite, and in crystals in which we observe Si–Be disorder. The Si occupancy converges stably to full site occupancy. The resulting occupancy parameters are given in Table 3. Final refinement position and occupancy parameters are given in Supplementary Table S4.

The relationship of the resulting site-scattering sum for Y1, Y2 and Y3 for all five samples, compared to the predicted site scattering from the EMP analyses determined from same locations is shown in Table 4 with weighted spatial

TABLE 3. Occupancies for thalénite-(Y) using ionic scattering factors.

Site	Samples	$Y_3Si_3O_{10}F$	GH-01	WC-G5	WC-X5	WC-X7	RS104
Y1	SOF-Yb		0.563(5)	0.581(7)	0.582(9)	0.578(7)	0.602(10)
	Electrons	36	37.72	38.93	38.99	38.73	40.33
Y2	SOF-Yb		0.585(5)	0.611(7)	0.615(9)	0.615(8)	0.651(11)
	Electrons	36	39.20	40.94	41.21	41.21	43.62
Y3	SOF-Yb		0.572(5)	0.593(7)	0.570(9)	0.576(7)	0.620(11)
	Electrons	36	38.32	39.73	38.19	38.59	41.54
Si1	SOF-Si		0.996(15)	1.00(2)	0.99(3)	0.99(2)	0.99(3)
	Electrons	10	10.0	10.0	9.9	9.9	9.9
Si2	SOF-Si		0.994(14)	1.02(2)	0.96(3)	0.96(2)	1.01(3)
	Electrons	10	9.9	10.2	9.6	9.6	10.1
Si3	SOF-Si		0.985(14)	0.99(2)	0.99(3)	0.94(2)	1.04(3)
	Electrons	10	9.9	9.9	9.9	9.4	10.4
O1-10	SOF-O		1 (fixed)	1 (fixed)	1 (fixed)	1 (fixed)	1 (fixed)
	Electrons	10	10	10	10	10	10
F1	SOF-F		1 (fixed)	1 (fixed)	1 (fixed)	1 (fixed)	1 (fixed)
	Electrons	10	10	10	10	10	10

SOF – site occupancy factor

TABLE 4. Y-site (Y1, Y2 and Y3) scattering from XRD and predicted site scattering (in electrons pfu) based on EMP analyses.

	Site scattering	Predicted site scattering[a]
$Y_3Si_3O_{10}F$	108	108
GH-01	115.2	119.24
WC-G5	119.6	120.24
WC-X5	118.4	120.6
WC-X7	118.5	120.6
RS104	125.5	125.29

[a] Predicted site scattering for GH-01, WC-G5 and RS104 are from the bulk averages given in Table 2. Predictions for WC-X5 and WC-X7 were generated from select EMP analytical points which were taken in the same area where the crystals for XRD were extracted.

compositional average considering zoning and heterogeneities extrapolated. A good agreement is seen within the uncertainly of ca. ±1 electron per *REE* site from XRD, and 1–2% electrons pfu uncertainty from EMP.

Raman spectroscopy

The representative Raman spectra of thalénite-(Y) for both localities for 632 nm excitation is shown in Fig. 8. Raman spectra were also acquired at 532 nm excitation; when plotting both the 532 nm and 632 nm spectral intensity *vs*. Raman shift, the primary peaks (200–1200 cm^{-1}) overlapped. This overlap is indicative of fluorescence as opposed to Raman emission with notable similarity for the material from both localities. In contrast, the emission in the 3000–3600 cm^{-1} region can be assigned to OH-stretch Raman emission. Distinct water modes are observed in all White Cloud samples investigated. No OH or H_2O vibrational mode is seen in the Golden Horn thalénite-(Y). No fluid inclusions could be identified, and the Raman spectra are reproducible across extended sample regions without any significant spectral variations. The water spectra are fit by four Gaussians with 3097, 3181, 3359 and 3526 cm^{-1} centre frequencies. The dominant peak centred around 3181 cm^{-1} is indicative of hexagonal water ice, while weaker but still strong peaks at 3359 and 3526 cm^{-1} indicate liquid H_2O. This suggests a superposition of a liquid and an ice-like feature, possibly in spatially nano-confined regions (Đuričković *et al*., 2011; Sun and Zheng, 2009).

Discussion

Of the three *REE* sites, only Y1 has bonds to the bridging oxygens, O4 and O7. Y1 has one long bond to the bridging oxygen O7 at > 2.7 Å as well as a very long bond to O4 at > 2.9 Å, whereas all other Y–O and Y–F bonds are between 2.2 and 2.6 Å, see Table 5 for select Y-site bond distances. From the distribution of electron densities in our natural thalénites-(Y) we conclude that the *REE* are ordered among the three Y-sites with the *Ln* cations showing a consistent enrichment at Y2 over Y1 and Y3. This is consistent with the shorter Y2–O and Y2–F bonds and associated smaller site volume giving preference for the occupation with smaller

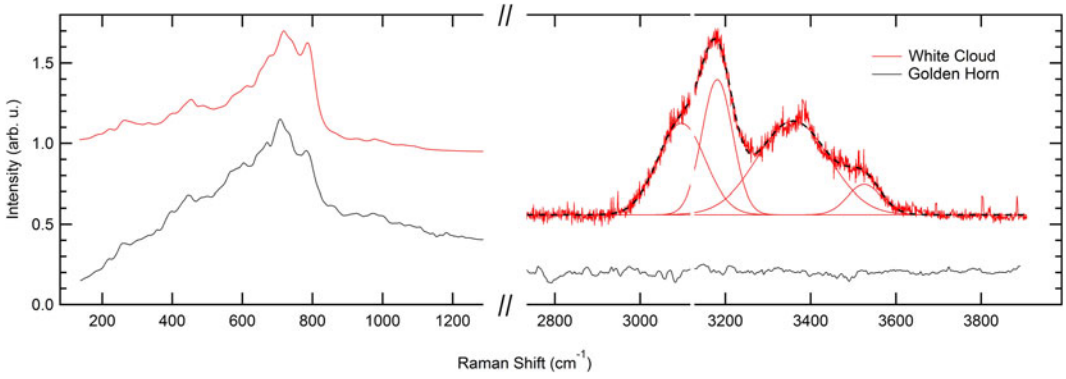

FIG. 8. Raman spectra for the Golden Horn and White Cloud thalénite-(Y) for 632 nm excitation, with an absence of OH and water in the Golden Horn thalénite-(Y), but the distinct presence of ice- and liquid-like water in White Cloud thalénite-(Y).

TABLE 5. Selected bond distances (Å) and averages for the three Y sites.

	$Y_3Si_3O_{10}F$[a]	GH-01	WC-G5	WC-X5	WC-X7	RS104
Y1–O2	2.24	2.245(5)	2.255(10)	2.242(12)	2.264(11)	2.265(15)
Y1–O2	2.256	2.256(6)	2.265(10)	2.272(12)	2.269(12)	2.276(16)
Y1–F	2.259	2.265(5)	2.273(9)	2.261(10)	2.278(10)	2.271(13)
Y1–O10	2.262	2.271(7)	2.286(9)	2.256(11)	2.273(11)	2.257(16)
Y1–O8	2.305	2.294(6)	2.290(9)	2.278(12)	2.288(12)	2.295(14)
Y1–O6	2.411	2.395(6)	2.392(10)	2.390(11)	2.385(11)	2.412(16)
Y1–O7	2.725	2.706(6)	2.746(10)	2.744(12)	2.736(12)	2.795(16)
Y1–O4	2.93	2.945(6)	2.964(10)	2.963(14)	2.997(13)	2.993(17)
<Y1–O6 F> [b]	2.35(6)	2.35(6)	2.36(6)	2.35(6)	2.36(6)	2.37(7)
Y2–O5	2.212	2.216(6)	2.230(10)	2.201(13)	2.202(12)	2.246(14)
Y2–O6	2.242	2.239(5)	2.214(10)	2.240(13)	2.228(12)	2.263(15)
Y2–O3	2.239	2.243(6)	2.256(10)	2.249(12)	2.271(11)	2.277(15)
Y2–O10	2.266	2.263(6)	2.266(11)	2.291(11)	2.265(10)	2.300(15)
Y2–O8	2.345	2.346(6)	2.367(9)	2.351(11)	2.346(11)	2.366(16)
Y2 – F	2.357	2.359(6)	2.364(8)	2.342(11)	2.335(12)	2.376(15)
Y2–O1	2.453	2.434(6)	2.464(10)	2.465(11)	2.458(10)	2.481(15)
<Y2–O6 F>	2.30(3)	2.30(3)	2.31(3)	2.31(3)	2.30(3)	2.33(3)
Y3 – F	2.24	2.242(5)	2.234(9)	2.237(10)	2.252(10)	2.226(13)
Y3–O9	2.288	2.279(6)	2.299(9)	2.305(12)	2.286(11)	2.265(16)
Y3–O1	2.286	2.301(6)	2.289(9)	2.284(11)	2.289(11)	2.310(16)
Y3–O3	2.316	2.323(6)	2.348(10)	2.336(13)	2.318(12)	2.335(14)
Y3–O9	2.334	2.349(6)	2.346(10)	2.368(13)	2.344(12)	2.347(13)
Y3–O5	2.391	2.387(7)	2.419(11)	2.413(13)	2.394(12)	2.426(16)
Y3–O1	2.586	2.587(6)	2.594(10)	2.582(13)	2.569(12)	2.644(15)
<Y3–O6 F>	2.35(4)	2.35(4)	2.36(4)	2.36(4)	2.35(4)	2.36(5)

[a] Schleid and Müller-Bunz (1998)
[b] The ~3.00 Å values of Y1–O4 were omitted from the averages for better comparison to Y2 and Y3.

HREE compared to the occupation of the larger Y1 and Y3 sites with lighter and larger *REE*. We calculated the electrostatic potentials for the various cation and anions sites in the structure using the structure data reported by Schleid and Müller-Bunz (1998) (Supplementary Table S3). We used the Bertaut method code *ELEN* described by Smyth (1988). Electrostatic potentials thus calculated are 30.8 V, 31.5 V and 29.7 V, for the Y1, Y2 and Y3 sites, respectively. The associated observed enrichment of *HREE* in the Y2 site is consistent with enrichment of heavier oxygen isotopes at sites of deeper electrostatic potentials (Smyth, 1988; Smyth and Clayton, 1988).

With regards to chemical composition, Ca and Al were historically reported at 2 wt.% oxide in White Cloud thalénite-(Y) analyses by Adams and Sharp (1972) and Adams *et al.* (1962). However, these high values are possibly due to impurities and inclusions of Ca and Al-bearing minerals, e.g. allanite-(Ce) and fluorite. More recent work of Wayne (1986) and Škoda *et al.* (2015) only detect traces of Ca and no Al in thalénite-(Y). This, together with our analyses suggests that Ca can be accommodated intrinsically into thalénite-(Y) to some extent by minor substitution for Y (as for 'yttrofluorite'), yet the minor presence of Al is more likely to be due to inclusions of other minerals.

Thalénite-(Y) is a primary magmatic mineral in many pegmatitic occurrences (e.g. Österby, Åskagen, Reunavare and Guy Hazel Claim, etc.) but it is prone to late-stage hydrothermal alteration and is often replaced by a second generation of thalénite-(Y), iimoriite-(Y), allanite-(Ce) and other *REE* minerals (Škoda *et al.*, 2015). The origin of thalénite-(Y) associated with Y-rich fluorite might be uncertain. While previous work (Haynes, 1965; Adams and Sharp, 1972; Simmons and Heinrich 1980) described the occurrence of thalénite-(Y) and other *REE* minerals at the White Cloud as being in 'replacement zones', recent advances in understanding of pegmatite petrogenesis and new field

work suggest that these zones rather represent a combination of late-magmatic and hydrothermal processes in which the magmatic crystallization sequence concentrates F, OH and *REE* into a low-viscosity F-rich fluid from which fluorite and *REE* minerals precipitate (Veksler *et al.*, 2005; Peretyazhko and Savina, 2010). In the final stages of crystallization from this F-rich fluid, fluorite and primary *REE* minerals such as gadolinite-(Y), allanite-(Ce), fergusonite-(Y), zircon and possibly thalénite-(Y) form. Later, possibly hydrothermal *REE* mineralization is characterized by replacement of primary fluorite by Y-rich fluorite, synchysite-(Y), thalénite-(Y) and fluocerite-(Ce), as well as replacement of gadolinite-(Y) by bastnäsite-(Ce), and Fe-oxide and clay replacement of biotite (Haynes 1965; Wayne 1986).

Adams and Sharp (1972) proposed that thalénite-(Y) in the White Cloud pegmatite could have formed due to an increase in SiO_2 and CO_2 during the hydrothermal stage, leading to the replacement of pre-existing *HREE* and Y-enriched fluorite by thalénite-(Y) and synchysite-(Y). They suggest that this hydrothermal fluid lacked PO_4 and did not crystallize multiple oxide *REE* phases (e.g. samarskite or euxenite), which might otherwise accommodate *HREE* and Y. Wayne (1986) suggested *HREE*, complexed with F, was partitioned into the final *REE* minerals to crystallize, and in some cases replace earlier *REE* minerals, such as gadolinite-(Y) and Y-bearing fluorite, so called 'yttrofluorite'. Wayne (1986) also suggested, on the basis of textural evidence, that thalénite-(Y) precipitated simultaneously with highly *HREE* and Y-enriched fluorite from the same residual fluid. At the White Cloud pegmatite, primary *REE* silicates gadolinites (both Ce and Y-dominant) and thalénite-(Y) are *HREE* and Y-enriched, and relatively depleted in Ce and La, which instead resides in lesser amounts of *REE* carbonates and fluorocarbonates such as synchysite-(Y) and bastnäsite-(Ce) (Wayne, 1986). However, the most abundant *REE* silicate, allanite-(Ce), is *LREE*-enriched, so the proposal by Wayne (1986) that thalénite-(Y) crystallization was triggered by depletion of the *HREE*-enriched late-stage fluid in Be, ending gadolinite crystallization, seems more plausible. However, the differences in Eu-anomalies between Wayne (1986) and our analyses, the heterogeneities of thalénite-(Y) composition at different scales, and the range of different *REE* mineral assemblages distributed widely across the pegmatite suggest multiple generations of thalénite-(Y), probably ranging from late-magmatic to hydrothermal to late fluid-driven alteration with attendant localized *REE* remobilization. The subtle tetrad effect, most pronounced in the Yb-rich thalénite-(Y) zones, supports different generations of late-stage fractionation from a hydrothermal F-rich fluid.

In contrast, the distinct oscillatory zoning of *HREE* in thalénite-(Y) from Golden Horn, a consistent tetrad effect, and its association with other late-stage minerals (annite, wulfenite, zircon, 'pyrochlore' and *REE* carbonates), supports the interpretation of a single late-stage hydrothermal process in the relatively closed-system environment of a miarolitic cavity with limited *REE*, Ca, P and F availability. The depletion of heaviest *HREE* as seen in the Golden Horn thalénite-(Y) is similar to observations for second generation of thalénite-(Y) from Österby (Škoda *et al.*, 2015), which were formed from primary magmatic thalénite-(Y) during hydrothermal alteration by a dissolution and *in situ* reprecipitation process as suggested by Putnis and Putnis (2007). Taking into account the hydrothermal origin, the absence of OH in the Golden Horn thalénite-(Y) is interesting and suggests crystallization from an F-bearing fluid. Experimental attempts of hydrothermal synthesis of Y-silicates from a F-absent environment only resulted in keiviite- or yttrialite-like $Y_2Si_2O_7$ (Fitzpatrick and Pabst, 1986; Becerro *et al.*, 2003). Our work, however, does not allow for the definite resolution of the question of the range of conditions of thalénite-(Y) formation. A more detailed petrological investigation of the full mineral assemblage and crystallization sequence together with analysis of the other *REE* minerals across the White Cloud pegmatite or Golden Horn miaoloitic cavities would be required to draw further conclusions regarding the petrogenesis of thalénite-(Y) at both localities.

Acknowledgements

We thank the reviewers Ritsuro Miyawaki and Peter Leverett for insightful suggestions about the manuscript. We are indebted to Mark Jacobson for sharing invaluable information about the pegmatites of the South Platte district. William (Skip) Simmons, Sarah Hanson, Dave London and Chuck Stern are acknowledged for helpful discussions about pegmatite mineralogy and petrogenesis. We acknowledge funding from NSF EAR-1427626 and the University of Colorado Boulder for acquisition of the JEOL JXA-8230 microprobe.

Supplementary material

To view Supplementary material for this article, please visit https://doi.org/10.1180/minmag.2017.081.044

References

Angel, R.J., Ross, N.L., Wood, I.G. and Woods, P.A. (1992) Single crystal X-ray diffraction at high pressures with diamond-anvil cells. *Phase Transitions*, **39**, 13–32.

Adams, J.W. and Sharp, W.H. (1972) Thalénite-(Y) and allanite derived from yttrofluorite in the White Cloud pegmatite, South Platte area, Colorado. *U.S. Geological Survey Professional Paper*, **800-C**, 63–69 pp. U.S. Geological Survey, Reston, Virginia, USA.

Adams, J.W., Hildebrand, F.A. and Havens, R.G. (1962) Thalenite from Teller County, Colorado. *United States Geological Survey Professional Paper*, **450-D**, 6–8 pp. U.S. Geological Survey, Reston, Virginia, USA.

Armbruster, T., Bonazzi, P., Akasaka, M., Bermanec, V., Chopin, C., Gieré, R., Heuss-Assbichler, S., Liebscher, A., Menchetti, S., Pan, Y. and Pasero, M. (2006) Recommended nomenclature of epidote-group minerals. *European Journal of Mineralogy*, **18**, 551–567.

Azavant, P. and Lichanot, A. (1993) X-ray scattering factors of oxygen and sulphur ions: an *ab initio* Hartree-Fock calculation. *Acta Crystallographica*, **A49**, 91–97.

Bačík, P., Miyawaki, R., Atencio, D., Cámara, F. and Fridrichová, J. (2018) Nomenclature of the gadolinite supergroup. *European Journal of Mineralogy*, **29**, 1067–1082.

Becerro, A.I., Naranjo, M. and Perdigón, A.C. and Trillo, J.M. (2003) Hydrothermal chemistry of silicates: low-temperature synthesis of y-yttrium disilicate. *Journal of the American Ceramic Society*, **86**, 1592–1594.

Becker, R. (1991) Minerals of the Golden Horn Batholith, Okanogan County, Washington. *Rocks and Minerals*, **66**, 453–458.

Benedicks, C. (1898) Mötet den 3 November 1898 [Thalénit, från Österby i Dalarne]. *Geologiska Föreningens i Stockholm Förhandlingar*, **20**, 308–312

Benedicks, C. (1900) Thalenit, ein neues Mineral aus Osterby in Dalekarlien. *Bulletin of the Geological Institution of the University of Uppsala*, **4**, 1–15.

Boggs, R.C. (1980) Okanoganite, a new rare-earth borofluorosilicate from the Golden Horn batholith, Okanogan County, Washington. *American Mineralogist*, **65**, 1138–1142.

Boggs, R. (1984) *Mineralogy and Geochemistry of the Golden Horn Batholith, North Cascades, Washington*. PhD dissertation, University of California, Santa Barbara, USA.

Boggs, R.C. (1988) Calciohilairite: $CaZrSi_3O_9\ 3H_2O$, the calcium analogue of hilairite from the Golden Horn Batholith, northern Cascades, Washington. *American Mineralogist*, **73**, 1191–1194.

Cromer, D.T. and Mann, J. (1968) X-ray scattering factors computed from numerical Hartree-Fock wave functions. *Acta Crystallographica*, **A24**, 321–323.

Đuričković, I., Claverie, R., Bourson, P., Marchettic, M., Chassot, J. M. and Fontana, M. (2011) Water-ice phase transition probed by Raman Spectroscopy. *Journal of Raman Spectroscopy*, **42**, 1408–1412.

Eddy, E.P., Bowring, S.A., Miller, R.B. and Tepper, J.H. (2016) Rapid assembly and crystallization of a fossil large-volume silicic magma chamber. *The Geology Society of America*, **44**, 331–334.

Fitzpatrick, J. and Pabst, A. (1986) Thalenite from Arizona. *American Mineralogist*, **71**, 188–193.

Frost, C.D. and Frost, B.R. (1997). High-K, iron-enriched rapakivi-type granites: the tholeiite connection. *Geology*, **25**, 647–650.

Griffin, W.L., Nilssen, B. and Jensen, B.B. (1979) Britholite CD and its alteration: Reiarsdal, Vest-Agder, south Norway. *Norsk Geologisk Tidsskrift*, **58**, 265–271.

Gonzáles del Tánago, J., La Iglesia, A. and Delgado, A. (2006) Kamphaugite-(Y) from La Cabrera massif, Spain: a low-temperature hydrothermal Y-REE carbonate. *Mineralogical Magazine*, **70**, 379–404.

Haynes, C.V., Jr. (1965) Genesis of the White Cloud and related pegmatites, South Platte area, Jefferson County, Colorado. *GSA Bulletin*, **76**, 441–461.

Kornev, A.N., Batalieva, N.G., Maksimov, B.A., Ilyukhin, V.V. and Belov, N.V. (1972) Crystal structure of thalénite-(Y) $Y_3[Si_3O_{10}](OH)$. *Soviet Physics Doklady*, **17**, 88–90, [translated from *Doklady Akademii Nauk SSSR*, **202**, 1324–1327, 1972].

Kozireva, I.V., Svecova, I.V. and Popova, T.N. (2004) Occurrence of Nd thalenite in Pripolar Ural. *Vestnik*, **6**, 2–3.

Kristiansen, R. (1993) Thalenitt-liknende mineraler fra Åskagen, Sverige. *Stein*, **1**, 59–60.

Mills, S.J., Hatert, F., Nickel, E.H. and Ferraris, G. (2009) The standardisation of mineral group hierarchies: application to recent nomenclature proposals. *European Journal of Mineralogy*, **21**, 1073–1080.

Minakawa, T., Noto, S. and Morioka, H. (1999) Rare earth minerals in Shikoku, with special reference to the occurrence of rare earth minerals in pegmatites in Ryoke and Hiroshima granites. *Memoirs of the Faculty of Science, Ehime University*, **5**, 1–32.

Misch, P. (1966) Tectonic evolution of the Northern Cascades of Washington State, in: Symposium on the tectonic history, mineral deposits of the western Cordillera: *Canadian Institute of Mining and Metallurgy Special Publication*, **8**, 101–148.

Müller-Bunz, H. and Schleid, T. (2000) Synthesis and constitution of fluorothalenite-type ($Y_3F[Si_3O_{10}]$) fluoride catena-trisilicates $M_3F\ [Si_3O_{10}]$ with the

lanthanides (M = Dy, Ho, Er). *Zeitschrift für anorganische und allgemeine Chemie*, **626**, 845–852.

Nagashima, K. and Kato, A. (1966) Chemical studies of minerals containing rarer elements from the Far East District. LX. Thalénite-(Y) from Suishoyama, Kawamata-machi, Fukushima Prefecture, Japan. *Bulletin of the Chemical Society of Japan*, **39**, 4–7.

Peretyazhko, I.S. and Savina, E.A. (2010) Tetrad effects in the rare earth element patterns of granitoid rocks as an indicator of fluoride-silicate liquid immiscibility in magmatic systems. *Petrology*, **18**, 514–543.

Putnis, A. and Putnis, C.V. (2007). The mechanism of reequilibration of solids in the presence of a fluid phase. *Journal of Solid State Chemistry*, **180**, 1783–1786.

Raade, G. and Kristiansen, R. (2009) Fluorthalénite-(Y) from Hundholmen, Tysfjord, north Norway. *Norsk Bergverksmuseum skrift* [letters of the Norwegian Museum of Natural History], 41–21.

Schleid, T. and Müller-Bunz, (1998) Einkirstalle von $Y_3F[Si_3O_{10}]$ im Thalenit-Typ. *Zeitschrift für anorganische Chemie*, **624**, 1082–1084.

Sheldrick, G.M. (2008) A short history of SHELX. *Acta Crystallographica*, **A64**, 112–122.

Simmons, W.B., Jr. and Heinrich, E.W. (1975) A summary of the petrogenesis of the granite-pegmatite system in the northern end of the Pikes Peak batholith: *Fortschritte der Mineralogie*, **52**, 251–264.

Simmons, W.B., Jr. and Heinrich, E.W. (1980) Rare earth pegmatites of the South Platte District, Colorado. *Colorado Geological Survey Resource Series*, **11**, 131.

Škoda, R., Plášil, J., Jonsson, E., Čopjaková, R., Langhof, J. and Vašinová Galiová, M. (2015) Redefinition of thalénite-(Y) and discreditation of fluorthalénite-(Y): A re-investigation of type material from the Österby pegmatite, Dalarna, Sweden, and from additional localities. *Mineralogical Magazine*, **79**, 965–983.

Smith, D.R., Noblett, J., Wobus, R.A., Unruh, D., Douglass, J., Beane, R., Davis, C., Goldman, S., Kay, G., Gustavson, B., Saltoun, B. and Stewart, J. (1999) Petrology and geochemistry of late-stage intrusions of the A-type, mid-Proterozoic Pikes Peak batholith (Central Colorado, USA): implications for petrogenesis models. *Precambrian Research*, **98**, 271–305.

Smyth, J.R. (1988) Electrostatic characterization of oxygen sites in minerals. *Geochimica et Cosmochimica Acta*, **53**, 1101–1110.

Smyth, J.R. and Clayton, R.N. (1988) Correlation of electrostatic site potentials with oxygen isotope fractionation in silicates. *EOS Trans American Geophysical Union*, **69**, 1514.

Stepanov, A.V., Bekenova, G.K., Levin, V.L., Sokolova, E., Hawthorne, F.C. and Dobrovol'skaya, E.A. (2012) Tarbagataite, $(K,\square)_2(Ca,Na)(Fe^{2+},Mn)_7Ti_2(Si_4O_{12})_2O_2(OH)_4(OH,F)$, a new astrophyllite-group mineral species from the Verkhnee Espe deposit, Akjailyautas mountains, Kazakhstan: Description and crystal structure. *The Canadian Mineralogist*, **50**, 159–168.

Stull, R. (1969) *The Geochemistry of the Southeastern Portion of the Golden Horn Batholith, Northern Cascades, Washington*. PhD dissertation, University of Washington, USA.

Sun, Q. and Zheng, H. (2009) Raman OH stretching vibration of ice I_h. *Progress in Natural Science*, **19**, 1651–1654.

Veksler, I.V., Dorfman, A.M., Kamenetsky, M., Dulski, P. and Dingwell, D.B. (2005) Partitioning of lanthanides and Y between immiscible silicate and fluoride melts, fluorite and cryolite and the origin of the lanthanide tetrad effect in igneous rocks. *Geochimica et Cosmochimica Acta*, **69**, 2847–2860.

Voloshin, A.V. and Pakhomovskii, Y.A. (1997) Fluorthalénite-(Y) – a new mineral from the amazonitic randpegmatites of the Kola Peninsula. *Doklady Akademii Nauk*, **354**, 77–78.

Vorma, A., Ojanperä, P., Hoffren, V., Siivola, J. and Löfgren, A. (1966) On the rare earth minerals from the Pyörönmaa pegmatite in Kangasala. *Comptes Rendu de la Société Geologique de Finlande*, **38**, 241–274.

Wayne, D.M. (1986) *Electron microprobe analysis of rare-earth-element-bearing phases from the white cloud pegmatite, South Platte district, Jefferson County, Colorado*. PhD Thesis, University of New Orleans, USA.

Williams, P.A., Hatert, F., Pasero, M. and Mills, S.J. (2014) IMA Commission on New Minerals, Nomenclature and Classification (CNMNC) Newsletter No. 22. *Mineralogical Magazine*, **78**, 1241–1248.

Yakubovich, O.V., Voloshin, A.V., Pakhomovskii, Ya.A. and Simonov, M.A. (1988) Refined crystal structure of thalenite. *Soviet Physics, Crystallography*, **33**, 356–358. [Original in Russian: *Kristallografiya*, **33**, 605–608 (1988)].